Single-Molecule Lysozyme Dynamics Monitored by an Electronic Circuit

Yongki Choi, *et al.*

Science **335**, 319 (2012);
DOI: 10.1126/science.1214824

tion with the advent of aberration correctors. The aberration-corrected ETEM images in Fig. 2, B and C, were therefore analyzed quantitatively as summarized in fig. S6. The imaging of adsorbed molecules of CO was thus further supported (*24*). As shown in a plan view (Fig. 2E) and a cross-sectional view (Fig. 2F) of this model, the CO molecules were adsorbed at the on-top sites of half the Au atoms in the undulating hexagonal lattice. The adsorption energy per CO molecule for this model was estimated to be 0.26 eV. Surface coverages exceeding 50% in the undulating hexagonal lattice were energetically unfavorable.

Previous theoretical studies (*22*, *23*, *30*) examined the adsorption of CO molecules onto unreconstructed GNP surfaces. CO molecules adsorb more strongly than oxygen molecules onto the surface of GNPs. Unlike ordinary Pd and Pt catalysts, it was thought that a flat facet of a GNP cannot accommodate CO molecules in high density (*20*, *21*) because of the intrinsic weak adsorption of a CO molecule and the repulsive interactions between CO molecules. CO molecules were thought to be adsorbed onto low-coordination sites such as steps, edges, and corners more strongly than a flat facet. However, the present aberration-corrected ETEM observation combined with ab initio calculations revealed that the surface structure of the {100} facets undergoes modifications that allow CO molecules to adsorb at higher surface coverages. In the Au{100}-hex reconstructed surface, the Au atoms on the topmost layer have unusual bonding configurations with the Au atoms on the second surface layer (*24*). The adsorption of CO molecules in high density can be sustained on the reconstructed surface. Reconstruction was not observed on the {111} facet of GNPs during our observations. According to theoretical studies, tensile stress is known to be induced onto the {100} facet more strongly than the {111} facet (*31*, *32*). In addition, the surface energy is higher in the {100} facet than in the {111} facet. Correspondingly, only long-range reconstruction is observed experimentally on the {111} facet (*33*–*35*). Therefore, a high affinity for CO adsorption is induced on the {100} facet of GNPs through reconstruction, whereas the stable {111} surface is considered to be oblivious to the presence of CO gas. Hence, along with previous studies, we have now obtained an atomistic view about the adsorption of CO molecules onto the supported GNP catalysts. Accumulated experimental data (*36*, *37*) indicate that the active sites of the GNP catalysts are located at the particle-support periphery where gas species such as O_2 or -OH probably react with CO. The methodology demonstrated in this study has opened an experimental route toward the elucidation of GNP catalytic mechanisms by direct observation of metal atoms and gas species at the particle-support periphery.

References and Notes

1. M. Haider *et al.*, *Nature* **392**, 768 (1998).
2. Y. Oshima *et al.*, *J. Electron Microsc.* **59**, 457 (2010).
3. J. C. Meyer *et al.*, *Nano Lett.* **8**, 3582 (2008).
4. C. L. Jia, M. Lentzen, K. Urban, *Science* **299**, 870 (2003).
5. Y. Oshima *et al.*, *Phys. Rev. B* **81**, 035317 (2010).
6. J. E. Allen *et al.*, *Nat. Nanotechnol.* **3**, 168 (2008).
7. M. Koshino *et al.*, *Science* **316**, 853 (2007).
8. Z. Liu, K. Yanagi, K. Suenaga, H. Kataura, S. Iijima, *Nat. Nanotechnol.* **2**, 422 (2007).
9. E. D. Boyes, P. L. Gai, *Ultramicroscopy* **67**, 219 (1997).
10. P. L. Hansen *et al.*, *Science* **295**, 2053 (2002).
11. H. Yoshida, S. Takeda, *Phys. Rev. B* **72**, 195428 (2005).
12. H. Yoshida, S. Takeda, T. Uchiyama, H. Kohno, Y. Homma, *Nano Lett.* **8**, 2082 (2008).
13. R. Wang, P. A. Crozier, R. Sharma, J. B. Adams, *Nano Lett.* **8**, 962 (2008).
14. P. L. Gai, E. D. Boyes, *Microsc. Res. Tech.* **72**, 153 (2009).
15. T. W. Hansen, J. B. Wagner, R. E. Dunin-Borkowski, *Mater. Sci. Technol.* **26**, 1338 (2010).
16. H. Yoshida *et al.*, *Appl. Phys. Express* **4**, 065001 (2011).
17. M. Haruta, N. Yamada, T. Kobayashi, S. Iijima, *J. Catal.* **115**, 301 (1989).
18. M. Haruta, *Catal. Today* **36**, 153 (1997).
19. S. D. Gardner *et al.*, *Langmuir* **7**, 2135 (1991).
20. F. Boccuzzi *et al.*, *J. Catal.* **202**, 256 (2001).
21. M. Haruta, *CATTECH* **6**, 102 (2002).
22. M. Mavrikakis, P. Stoltze, J. K. Nørskov, *Catal. Lett.* **64**, 101 (2000).
23. L. M. Molina, B. Hammer, *Phys. Rev. B* **69**, 155424 (2004).
24. Materials and methods are available as supporting material on *Science* Online.
25. Y. J. Feng, K. P. Bohnen, C. T. Chan, *Phys. Rev. B* **72**, 125401 (2005).
26. T. Jacob, *Electrochim. Acta* **52**, 2229 (2007).
27. H. W. Zandbergen, C.-W. Pao, D. J. Srolovitz, *Phys. Rev. Lett.* **98**, 036103 (2007).
28. D. G. Fedak, N. A. Gjostein, *Surf. Sci.* **8**, 77 (1967).
29. T. Sasaki *et al.*, *J. Electron Microsc. (Tokyo)* **59** (suppl. 1), S7 (2010).
30. K. P. McKenna, P. V. Sushko, A. L. Shluger, *J. Chem. Phys.* **126**, 154704 (2007).
31. V. Fiorentini, M. Methfessel, M. Scheffler, *Phys. Rev. Lett.* **71**, 1051 (1993).
32. V. Zólyomi, L. Vitos, S. K. Kwon, J. Kollár, *J. Phys. Condens. Matter* **21**, 095007 (2009).
33. M. A. Van Hove *et al.*, *Surf. Sci.* **103**, 189 (1981).
34. K. Takayanagi, Y. Tanishiro, K. Yagi, K. Kobayashi, G. Honjo, *Surf. Sci.* **205**, 637 (1988).
35. J. V. Barth, H. Brune, G. Ertl, R. J. Behm, *Phys. Rev. B* **42**, 9307 (1990).
36. I. X. Green, W. Tang, M. Neurock, J. T. Yates Jr., *Science* **333**, 736 (2011).
37. T. Fujitani, I. Nakamura, *Angew. Chem. Int. Ed.* **50**, 10144 (2011).

Acknowledgments: This study was supported by a Grant-in-Aid for Specially Promoted Research, grant 19001005, from the Ministry of Education, Culture, Sports, Science and Technology, Japan.

Supporting Online Material

www.sciencemag.org/cgi/content/full/335/6066/317/DC1
Materials and Methods
Figs. S1 to S6
Movies S1 to S3
References (*38*–*53*)

25 August 2011; accepted 22 November 2011
10.1126/science.1213194

Single-Molecule Lysozyme Dynamics Monitored by an Electronic Circuit

Yongki Choi,[1,2*] Issa S. Moody,[3*] Patrick C. Sims,[2] Steven R. Hunt,[2] Brad L. Corso,[2] Israel Perez,[2] Gregory A. Weiss,[3,4†] Philip G. Collins[1,2†]

Tethering a single lysozyme molecule to a carbon nanotube field-effect transistor produced a stable, high-bandwidth transducer for protein motion. Electronic monitoring during 10-minute periods extended well beyond the limitations of fluorescence techniques to uncover dynamic disorder within a single molecule and establish lysozyme as a processive enzyme. On average, 100 chemical bonds are processively hydrolyzed, at 15-hertz rates, before lysozyme returns to its nonproductive, 330-hertz hinge motion. Statistical analysis differentiated single-step hinge closure from enzyme opening, which requires two steps. Seven independent time scales governing lysozyme's activity were observed. The pH dependence of lysozyme activity arises not from changes to its processive kinetics but rather from increasing time spent in either nonproductive rapid motions or an inactive, closed conformation.

Numerous experimental techniques have been developed to probe the dynamics of single molecules (*1*) and overcome the averaging effects of ensemble measurements. The most common experimental techniques use fluorescence, encoding molecular motions and/or chemical reactions into a highly amplified photon flux that can be monitored and analyzed (*2*, *3*). We show that single-molecule dynamics can be monitored by attaching the molecule of interest to a field-effect transistor (FET) device (Fig. 1A). Signal amplification was achieved by allowing the charged functionalities on the surface of the protein to electrostatically gate the underlying FET. By exploiting the low dimensionality and extreme local gate sensitivity of single-walled carbon nanotube (SWNT) FETs, molecular motions create changes in electrostatic potentials that can be converted into dynamically changing elec-

[1]Institute for Surface and Interface Science, University of California Irvine, Irvine, CA 92697–2375, USA. [2]Department of Physics and Astronomy, University of California Irvine, Irvine, CA 92697–4576, USA. [3]Department of Molecular Biology and Biochemistry, University of California Irvine, Irvine, CA 92697–4292, USA. [4]Department of Chemistry, University of California Irvine, Irvine, CA 92697–2025, USA.

*These authors contributed equally to this work.
†To whom correspondence should be addressed. E-mail: gweiss@uci.edu (G.A.W.); collinsp@uci.edu (P.G.C.)

tron fluxes. Such signals are similar to the photon fluxes in fluorescence experiments, but with advantageous bandwidth and shot noise limitations.

The general concept of electronic transduction by low-dimensional FETs has been explored with SWNT (*4*–*7*), silicon nanowire (*8*–*11*), nanocluster (*12*, *13*), and graphene (*14*–*16*) devices. In most cases, slow changes in DC conductance have been suggestive of single-molecule detection, but the absence of dynamic responses undermined the general premise of high bandwidth detection. Recently, high-bandwidth dynamic transduction has been achieved in two single-molecule electronic architectures. In the first, DNA molecules threading through solid state pores have generated high-fidelity electronic signals that offer opportunities for DNA sequencing (*15*, *16*). Separately, a more traditional FET architecture has leveraged amplification at SWNT point defects (*17*) to demonstrate kinetic binding and unbinding, both for molecules interacting directly with the defect site (*18*) and indirectly through an attached biomolecule (*19*, *20*).

Here, we accomplished single-molecule transduction very similar to the work of Sorgenfrei *et al*. (*19*, *20*), but using a noncovalent bioconjugation strategy that provides a high device-fabrication yield. Rather than introducing a defect, tailoring its chemistry, and then conjugating that site to the target molecule, our method used noncovalent immobilization based on pyrene linkers (*21*). The pyrenes adhered to SWNTs through pi-pi stacking, and could provide dilute anchor points for further derivatization of the surface (*22*–*24*). In our particular implementation, a thiol from a single cysteine variant of T4 lysozyme (S90C) was covalently conjugated to a pyrene-maleimide anchor site [see figs. S1 and S2 for characterization details (*25*)]. Similar site-specific conjugation of lysozyme to a solid surface has previously been shown to have no effect on the catalytic activity of lysozyme (*26*). Used here as a template for introducing the S90C substitution, the pseudo–wild-type mutant of lysozyme (C54T, C97A) has activity and stability identical to that of wild-type lysozyme (*27*). To minimize potential perturbations to the enzyme, lysozyme was not conjugated to a His_6 epitope, and was instead purified to >95% homogeneity by cation exchange followed by size exclusion chromatography. Standard biochemical conjugation protocols, followed by a strict rinsing protocol to minimize nonspecific binding, readily produced lysozyme attachments with a mean separation of 0.5 μm along the SWNT. Matching this empirical spacing to the SWNT channel length is a surprisingly simple method that produced active single-molecule devices in 8 out of 10 fabrication attempts.

Atomic force microscopy (AFM) before functionalization and after completion of the measurements (Fig. 1B) confirmed the presence of a single attached lysozyme. Lysozyme is ~7 nm in size, which made it easily distinguishable when attached to a 1- to 2-nm-diameter SWNT [see fig. S3 for additional examples and height profiles (*25*)]. In addition to microscopy, electrical characterization was performed at each fabrication stage. Figure 1C shows the gate dependence of the source-drain current $I(V_g)$ in a completed lysozyme device, measured with aqueous electrolyte (phosphate-buffered saline) in direct contact with the SWNT sidewall (*28*). The shape of this curve reflects SWNT band structure, contact resistance effects, and the role of scattering induced by the pyrenes and attached lysozyme; these issues are discussed in greater detail in the supporting online material (SOM) (*25*). In general, the coating technique added 1 to 2 megohms of series resistance to the SWNT conductor and shifts its $I(V_g)$ curve, in accord with previous reports (*4*, *29*, *30*). Finally, Fig. 1D displays the typical device response $I(t;\ V_g = 0)$ upon introduction of the lysozyme substrate, peptidoglycan (Sigma-Aldrich). A polysaccharide found in bacterial cell walls, peptidoglycan consists of *N*-acetylmuramate (NAM)–*N*-acetylglucosamine (NAG) repeating units, and lysozyme catalyzes the hydrolysis of its glycosidic bonds (*31*). Chemoresistive responses of this nature are widely reported for nanodevices, and SWNT conductance can be quite sensitive to slight environmental changes, even when they are not decorated with proteins (*32*–*34*).

The time-averaged, DC response depicted in Fig. 1D underlies the classification of such devices as chemical or biological "sensors." However, analysis of the dynamic response, not the DC level, can provide insights into conformational changes of the attached single protein. The magnitude of $I(t)$ fluctuations increased immediately when peptidoglycan substrate was added, and, after one or more seconds of equilibration, these fluctuations developed into a two-level, random telegraph signal (RTS) that can be statistically analyzed. Control experiments probing bare SWNTs [fig. S4 (*25*)] and lysozyme-free, pyrene-coated SWNTs [fig. S5 (*25*)] revealed no RTS response to peptidoglycan substrate; further controls included 12 devices fabricated with either of two, inactive variants of lysozyme [fig. S6 (*25*)], none of which exhibited RTS signals. In every experiment, the presence or absence of RTS fluctuations was a reliable predictor of the simultaneous presence of the peptidoglycan substrate and a SWNT-bound, catalytically functional variant of lysozyme.

Figure 2A shows 30 s of raw data collected from a single lysozyme device, along with the time-varying mean computed with a 10-Hz digital filter. The lowest-frequency fluctuations had a $1/f$ spectral dependence and were indistinguishable from the noise incurred by a pristine SWNT in solution. Removing this slowly changing component, as shown in Fig. 2B, greatly simplified further analysis. The higher-frequency components were revealed to be a two-level RTS with a constant amplitude distribution but two dis-

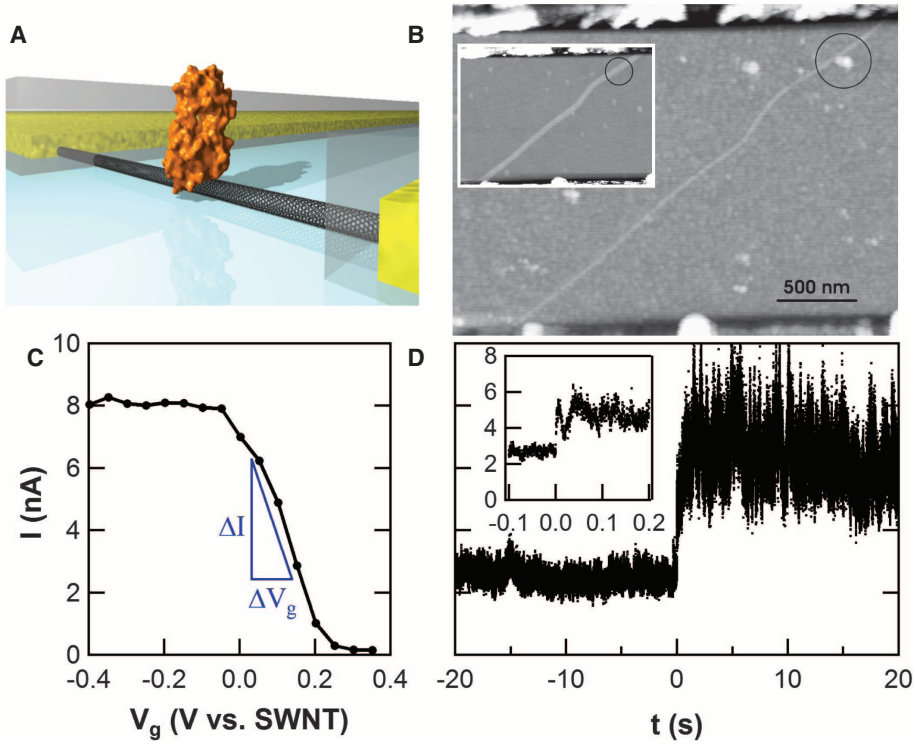

Fig. 1. (**A**) Schematic diagram of the single lysozyme being interrogated by a carbon nanocircuit. The partial poly(methyl methacrylate) coating is depicted in gray. (**B**) AFM topography of a SWNT FET before (inset) and after coating with the pyrene linker, lysozyme incubation, and washing to reduce nonspecific binding. The circle highlights the point of lysozyme attachment. (**C**) Response of current in a lysozyme device to electrolytic gating. (**D**) $I(t)$ measured in phosphate buffer, with peptidoglycan substrate (25 μg/ml) added to the solution at $t = 0$. The inset with a magnified time axis indicates a rapid response of <50 ms (inset).

tinct RTS fluctuation rates. During some time periods, the RTS oscillated with a "fast" mean frequency of 316 Hz (Fig. 2C). At other times, the RTS oscillated with a "slow" mean frequency of 15.4 Hz (Fig. 2D). The data in Fig. 2C are colored to differentiate the two types of RTS response and to emphasize their typical durations. Both the fast and the slow RTS segments lasted many seconds, suggestive of a long-term, two-state "memory" that was independent of the RTS itself. Accurate determination of the mean duration of this memory effect $\langle\tau_{mem}\rangle$ required that measurements be conducted for at least 600 s.

The sequences of fast and slow RTS oscillations could be separated for independent analysis. Each type of oscillation had a high and a low current state characterized by durations τ_{hi} and τ_{lo}, respectively. Probability distributions for τ_{hi} and τ_{lo} are shown for a sequence of fast RTS fluctuations in Fig. 3A and for slow RTS fluctuations in Fig. 3B; the color scheme corresponds to the data in Fig. 2, B to D. All four distributions were well fit by single exponential time constants for periods of analysis shorter than $\langle\tau_{mem}\rangle$. Analysis of much longer time periods resulted in biexponential distributions (Fig. 3, C and D) and reflected the presence in data sets extending over hundreds of seconds of many sequences of both fast and slow RTS fluctuations. However, the fast and slow rates were sufficiently different that they appeared as two distinguishable slopes in Fig. 3, C and D. As a guide, blue and green colors have been applied to portions of the distribution that correspond to the fast and slow fluctuations, respectively.

Figure 3, C and D, further provide a comparison of the probability distributions acquired at different pH values. The stability of the lysozyme devices allowed statistics to be accumulated for many minutes at each pH, all from the same attached enzyme. Figure 3C shows that τ_{hi} was nearly independent over a pH range from 5 to 11; outside this pH range, lysozyme was no longer catalytically active (*35*–*37*). Figure 3D, however, shows that τ_{lo} is much faster at pH 7 than at pH 5 or 11. The pH dependence of τ_{lo} in the long-duration, slow-switching region of the histogram, being much longer than the other three time constants, dominates the time-averaged properties of the lysozyme molecule.

Two important physical parameters could be calculated from the mean values of $\langle\tau_{lo}\rangle$ and $\langle\tau_{hi}\rangle$. Their sum represents one complete oscillation and defines a mean turnover rate for the activity, $k = (\langle\tau_{lo}\rangle + \langle\tau_{hi}\rangle)^{-1}$. The calculation of enzymatic reaction rates from single-molecule data has been reviewed by Xie (*38*). The ratio of $\langle\tau_{lo}\rangle$ and $\langle\tau_{hi}\rangle$ also determines an energy separation, ΔE, between the two physical states responsible for the high and low $I(t)$ values. Boltzman statistics provides the relative thermodynamic probability of being in one state versus the other as $\Delta E = k_B T \ln(\langle\tau_{hi}\rangle / \langle\tau_{lo}\rangle)$. In total, we identified five independent parameters $\langle\tau_{hi}\rangle$, $\langle\tau_{lo}\rangle$, $\langle\tau_{mem}\rangle$, k, and ΔE, all of which change when the lysozyme switches from its fast RTS state to its slow RTS state. Table 1 summarizes these parameters and their pH dependence for a single lysozyme molecule.

Table 1 further lists the overall percentage of time spent in the fast or slow RTS states. This percentage is yet another independent parameter, being a nontrivial combination of the duration $\langle\tau_{mem}\rangle$ and the regularity with which each behavior is observed. At pH 7, $\langle\tau_{mem}\rangle$ was nearly equal for the fast and the slow RTS state, and the time in either state approached 50%. At non-neutral pH values, however, multiple changes skewed this balance. First, the number of inactive periods in which no switching was observed nearly doubled. This doubling, amplified by a modest increase in $\langle\tau_{mem}\rangle$ of the inactive duration, resulted in a rapidly growing proportion of total inactive time. Moreover, we observed that inactive periods always interrupted sequences of fast RTS oscillations and doubled the number of fast RTS intervals observed while only modestly decreasing their duration $\langle\tau_{mem}\rangle$. The increased time spent in inactive or fast RTS intervals both came at a cost to the percentage of time spent in the slow-switching RTS state, which was reduced to 19.7% at pH 11 and 15.7% at pH 5. This decrease occurred despite a substantial increase in $\langle\tau_{mem}\rangle$, which considered in isolation would indicate an improving stability of the slow RTS state. We further note that the fast and slow RTS oscillation rates k both decreased by 25 to 35% away from pH 7; because they both decreased proportionally, the k values only minimally contributed to the pH dependence of the time spent in the fast or slow RTS states.

The conductance signal of a single lysozyme device allowed us to directly determine multiple independent parameters, including seven independent time constants and their pH dependence, all without foreknowledge of the properties of either the enzyme or the SWNT. Out of 50 single-

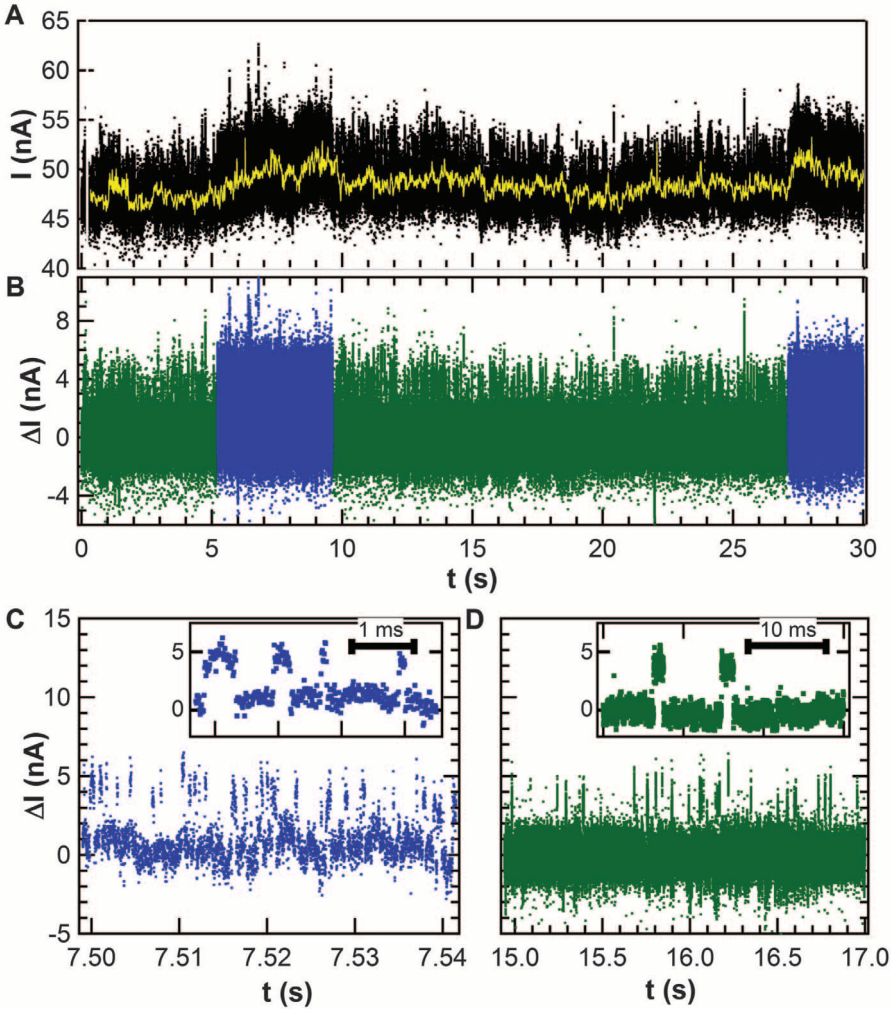

Fig. 2. (**A**) Long-duration $I(t)$ sequences exhibit dynamic noise on top of low-frequency fluctuations (yellow line) having a $1/f$ distribution. (**B**) Subtracting the meandering mean produces a filtered data set that clarifies the fluctuations as two-level, simplifies further analysis, and reveals that the two-level switching rates vary over 5- to 15-s periods. (**C**) The faster RTS oscillates about 300 times per second, whereas (**D**) the slower RTS oscillates 15 times per second. The insets show individual switching events for each case.

molecule devices, the presence of fast and slow RTS components was very reproducible, although there were variations in the numerical rates observed. For example, among seven lysozyme devices with high-quality signal-to-noise ratios, the rates of the slow RTS state at pH 7 varied from 10 to 50 Hz, with a mean $k = 24 \pm 15$ Hz. The rate of the fast RTS state varied from 127 to 461 Hz, with a mean $k = 284 \pm 127$ Hz.

Next, we applied these empirical observations to examine the mechanism and catalytic activity of lysozyme, through detailed analysis of the electronic device signal from lysozyme-tethered nanocircuits. As noted above and demonstrated in figs. S4 to S6 (*25*), the RTS can be ascribed to the presence of protein-substrate interactions. By comparing the $I(t)$ signal to lysozyme dynamics known from ensemble and single-molecule fluorescence resonance energy transfer (FRET) experiments (*39*–*42*), we can draw several parallels (e.g., lysozyme remains static in the absence of substrate). During substrate processing, lysozyme undergoes an 8 Å, hinge-like mechanical motion with two domains closing around the substrate (*41*–*45*). FRET observations reveal that this motion occurs at two different rates: a slow hinge oscillation of 20 to 90 Hz corresponding to enzymatic turnover events, or else a more rapid, nonproductive movement at 200 to 400 Hz (*37*, *41*, *42*).

These FRET rates are in excellent agreement with our fast RTS and slow RTS oscillations, and the interconversion rate matches our $\langle\tau_{mem}\rangle$ values. Thus, we conclude that the two-level electronic signal is caused by the lysozyme hinge motion, with slow RTS oscillations resulting from the transduction of catalytic turnover events and fast RTS oscillations corresponding to lysozyme's nonproductive binding events. These kinetic rates obtained with surface-bound lysozyme might differ from bulk rates, but FRET measurements with freely diffusing lysozyme and surface-bound peptidoglycan (*40*) yield the same range of rates, suggesting that the consequences of tethering the lysozyme to a surface are minor.

The agreement demonstrates the equivalence of the lysozyme device data with FRET measurements, but in other ways the SWNT-lysozyme device data are more informative. Fluorophore bleaching and quenching limit the duration of FRET measurements on a single molecule and constrain the ability to observe slow conformational interconversions by FRET (*37*). The $I(t)$ measurement duration is not similarly limited, and the $\langle\tau_{mem}\rangle$ values in Table 1 represent hundreds of such events by the same single molecule. Using such long time scales, we directly observed the same molecule changing from its productive conformation to its unproductive one. We also obtained the average percentage time spent in the slow RTS state, which when multiplied by k gave a time-averaged, effective catalytic rate for the single molecule. By collecting a true average over many conformational changes, this single-molecule rate approached the kinetics of an ensemble (Table 1). Furthermore, our $I(t)$ records extend this single-molecule insight to different pH conditions.

Measurements of a long-duration $\langle\tau_{mem}\rangle$ support a processive catalytic mechanism in which each lysozyme hydrolyzes on average 100 glycosidic bonds before dissociation and reassociation of the substrate (*40*). During the slow RTS state, no breaks in activity were observed, and so no product dissociation and substrate rebinding occurred. Furthermore, the substrate remained bound during both nonproductive fast RTS and the substrate-bound inactive state before returning to processing.

Our long-duration data sets also enable analysis of the statistical variance of the τ_{lo} and τ_{hi} values. Any single-step Poisson process has a statistical variance $\sigma^2 = \langle\tau\rangle^2$, and the normalized variance

$$r = \frac{\sigma^2}{\langle t\rangle^2} = \frac{\sum_i (\tau_i - \langle\tau\rangle)^2}{\sum_i \tau_i^2}$$

is a powerful tool in single-molecule studies for distinguishing hidden intermediate steps along a reaction coordinate (*46*–*48*). As shown in Table 2, analysis of individual τ_{lo} durations concludes that $r \approx 1$, indicating that the physical processes underlying the transition from I_{lo} to I_{hi} is in fact governed by a simple, single-step Poisson pro-

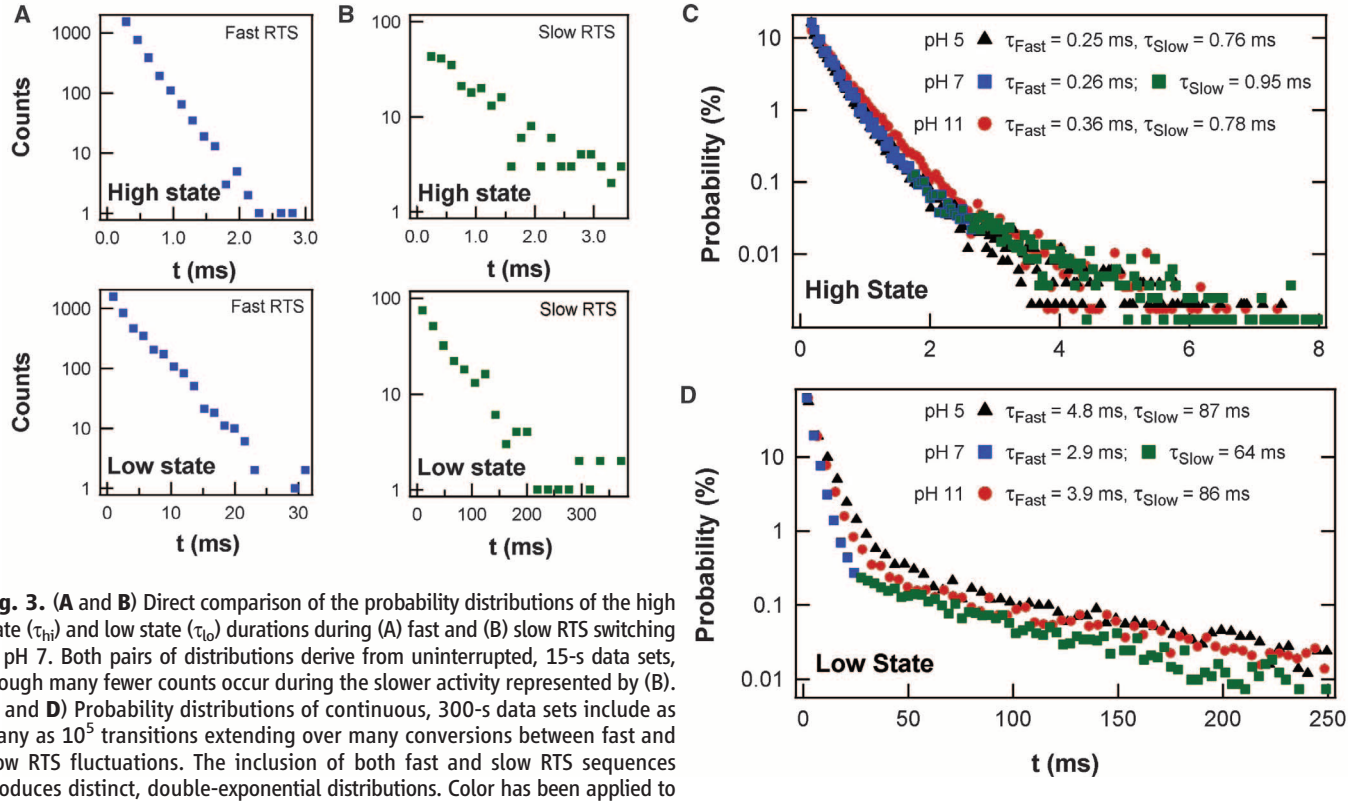

Fig. 3. (**A** and **B**) Direct comparison of the probability distributions of the high state (τ_{hi}) and low state (τ_{lo}) durations during (A) fast and (B) slow RTS switching at pH 7. Both pairs of distributions derive from uninterrupted, 15-s data sets, though many fewer counts occur during the slower activity represented by (B). (**C** and **D**) Probability distributions of continuous, 300-s data sets include as many as 10^5 transitions extending over many conversions between fast and slow RTS fluctuations. The inclusion of both fast and slow RTS sequences produces distinct, double-exponential distributions. Color has been applied to portions of the distributions in (A) to (D) to highlight correspondences with Fig. 2. Measurements at three different pH values show that the high-current state has almost no pH dependence (C). By contrast, the low-current state is at least 25% faster at pH 7 than at pH 5 or 11 (D).

cess. This conclusion remains true for both fast and slow RTS data at the different pH values tested, even though τ_{lo} differs by a factor of 20. By contrast, the physical process underlying the I_{hi} to I_{lo} transition has values of $r < 1$, indicating more complex processes. For example, n identical Poisson processes in succession will produce a distribution of durations τ that have a variance $r = 1/n$ (*47*, *49*). Thus, lysozyme forms a closed conformation in a single step, but the transition back to its open configuration requires at least two steps. Although this finding is the same for both fast and slow RTS oscillations, the extra intermediate step required for opening is not necessarily the same in both cases. During processive sequences, the intermediate step could play a role in the catalysis and substrate turnover (*50*). During fast sequences of nonproductive binding, it might be involved in repositioning the substrate within the active site in an attempt to find a reactive bond for hydrolysis. Notably, the inactive state of lysozyme occurs when the enzyme closes around the substrate.

Finally, we conclude with a brief discussion of the device's transduction mechanism. The current step that occurs with each opening and closing of the lysozyme is surely not additional carriers flowing into the SWNT from the protein or the electrolyte. The entire current $I(t)$ flows from source to drain electrode, with variability introduced by lysozyme's hinge-bending motion. The change from open to closed conformations moves lysozyme's charge residues (*51*). The surrounding electrolyte, which has a Debye length of 0.8 nm, screens most of the residues but not two, positively charged residues, Lys^{83} and Arg^{119}, that are located on the protein surface within 1.0 to 1.2 nm of the SWNT attachment site. Both of these residues lie close enough to the SWNT that their movement can electrostatically gate the channel conductance (*52*–*54*), according to the mechanism most often attributed to similar sensing experiments (*6*, *29*, *55*).

To test the applicability of this mechanism, we compared the transduction by different SWNT devices. Using the average slope dI/dV_g indicated in Fig. 1C, one can convert the RTS magnitude ΔI of a fluctuation into an effective swing in the applied gate, $\Delta V_g = \Delta I\,(dI/dV_g)^{-1}$. For the device in Fig. 2, for example, $\Delta I = 5$ nA and $\Delta V_g = 0.20$ V. Table S2 summarizes device properties of five semiconducting SWNT devices and five metallic ones, each having a different contact resistance and mean current (*25*). For these 10 devices, the switching magnitudes ΔI vary from 3 to 300%, but the calculated values ΔV_g are all narrowly clustered around $\Delta V_g = 0.19 \pm 0.02$ V. This reproducibility in ΔV_g demonstrates that the signal transduction mechanism is indeed electrostatic, with every protein-pyrene attachment modulating its underlying SWNT channel with the same effective field. Metallic SWNTs display the smallest ΔI signals, but only because of their modest sensitivity to gating.

It would be a mistake, however, to infer that the lysozyme is gating the entire SWNT, or to convert ΔV_g into a carrier concentration. The pyrene-protein attachment site is a highly localized scattering center that, because the SWNT is quasi-one dimensional, can modulate the entire channel conductance. The resistance increase that occurs upon conjugation (table S2) is believed to be concentrated primarily at the attachment site, similar to the case of a defect being introduced (*17*–*19*). Scanning probe measurements prove these local scattering sites to be strongly gate-dependent conduction barriers (*56*). During substrate binding and release, the charged side chains of Lys83 and Arg119 move by 1 to 2 Å relative to the SWNT (*41*–*44*, *57*). This motion is sufficient to modulate the local chemical potential in the SWNT and account for our observed ΔI (*56*).

This nanocircuit architecture is complementary to more traditional fluorescence techniques, but with the advantages that fluorescent labels are not required, the transduction mechanism does not bleach, and electronic bandwidths extend temporal resolution into the single-microsecond regime. These advantages provide a framework for exploring dynamics of other molecules with charged functionalities.

Table 1. Lysozyme activity rates.

Parameter	pH 5	pH 7	pH 11
	Processing (slow)		
$\langle\tau_{hi}\rangle$ (ms)	0.76 ± 0.05	0.95 ± 0.08	0.78 ± 0.09
$\langle\tau_{lo}\rangle$ (ms)	87 ± 3.0	64 ± 2.0	86 ± 3.0
ΔE (kcal/mol)	2.84	2.53	2.82
k (Hz)	11.4	15.4	11.5
$\langle\tau_{mem}\rangle$ (s)	9.3 ± 5.1	8.0 ± 3.0	12.0 ± 4.4
% time in state	16.3%	41.1%	21.1%
Time-averaged catalytic rate (Hz)	1.8	6.3	2.4
	Nonproductive (fast)		
$\langle\tau_{hi}\rangle$ (ms)	0.25 ± 0.01	0.26 ± 0.01	0.36 ± 0.01
$\langle\tau_{lo}\rangle$ (ms)	4.80 ± 0.35	2.90 ± 0.10	3.90 ± 0.17
ΔE (kcal/mol)	1.77	1.45	1.43
k (Hz)	198	316	235
$\langle\tau_{mem}\rangle$ (s)	6.2 ± 4.0	7.9 ± 2.3	5.4 ± 1.8
% time in state	72.4%	52.1%	63.8%
	Inactive		
$\langle\tau_{mem}\rangle$ (s)	0.83 ± 0.63	0.72 ± 0.25	0.96 ± 0.53
% time in state	11.3%	6.8%	15.0%

Table 2. Normalized variances of lysozyme rates.

Parameter	pH 5	pH 7	pH 11
	Processing (slow)		
r_{hi}	0.68 ± 0.15	0.74 ± 0.12	0.60 ± 0.15
r_{lo}	1.00 ± 0.18	1.06 ± 0.15	1.11 ± 0.23
	Nonproductive (fast)		
r_{hi}	0.48 ± 0.10	0.43 ± 0.06	0.61 ± 0.08
r_{lo}	0.97 ± 0.13	0.99 ± 0.09	1.00 ± 0.10

References and Notes

1. S. A. Claridge, J. J. Schwartz, P. S. Weiss, *ACS Nano* **5**, 693 (2011).
2. W. Min *et al.*, *Acc. Chem. Res.* **38**, 923 (2005).
3. R. Roy, S. Hohng, T. Ha, *Nat. Methods* **5**, 507 (2008).
4. A. Star, J. C. P. Gabriel, K. Bradley, G. Gruner, *Nano Lett.* **3**, 459 (2003).
5. A. Star *et al.*, *Org. Lett.* **6**, 2089 (2004).
6. K. Besteman, J. O. Lee, F. G. M. Wiertz, H. A. Heering, C. Dekker, *Nano Lett.* **3**, 727 (2003).
7. G. Gruner, *Anal. Bioanal. Chem.* **384**, 322 (2006).
8. Y. Cui, Q. Q. Wei, H. K. Park, C. M. Lieber, *Science* **293**, 1289 (2001).
9. F. Patolsky *et al.*, *Proc. Natl. Acad. Sci. U.S.A.* **101**, 14017 (2004).
10. F. Patolsky *et al.*, *Science* **313**, 1100 (2006).
11. F. Patolsky, G. F. Zheng, C. M. Lieber, *Anal. Chem.* **78**, 4260 (2006).
12. S. J. Park, T. A. Taton, C. A. Mirkin, *Science* **295**, 1503 (2002).
13. Y. Xiao, F. Patolsky, E. Katz, J. F. Hainfeld, I. Willner, *Science* **299**, 1877 (2003).
14. F. Schedin *et al.*, *Nat. Mater.* **6**, 652 (2007).
15. S. Huang *et al.*, *Nat Nano* **5**, 868 (2010).
16. M. Tsutsui *et al.*, *Sci. Rep.* **1**, 1 (2011).
17. B. R. Goldsmith *et al.*, *Science* **315**, 77 (2007).
18. B. R. Goldsmith, J. G. Coroneus, A. A. Kane, G. A. Weiss, P. G. Collins, *Nano Lett.* **8**, 189 (2008).
19. S. Sorgenfrei *et al.*, *Nat Nano* **6**, 126 (2011).
20. S. Sorgenfrei, C. Y. Chiu, M. Johnston, C. Nuckolls, K. L. Shepard, *Nano Lett.* **11**, 3739 (2011).
21. R. J. Chen, Y. Zhang, D. W. Wang, H. J. Dai, *J. Am. Chem. Soc.* **123**, 3838 (2001).
22. A. B. Artyukhin, O. Bakajin, P. Stroeve, A. Noy, *Langmuir* **20**, 1442 (2004).
23. Y. L. Zhao, L. B. Hu, J. F. Stoddart, G. Gruner, *Adv. Mater.* **20**, 1910 (2008).
24. D. J. Perello *et al.*, *J. Appl. Phys.* **105**, 124309 (2009).

25. Materials, methods, and additional control data are available as supporting material on *Science* Online.
26. K. L. Heredia *et al.*, *J. Am. Chem. Soc.* **127**, 16955 (2005).
27. M. Matsumura, B. W. Matthews, *Science* **243**, 792 (1989).
28. S. Rosenblatt *et al.*, *Nano Lett.* **2**, 869 (2002).
29. R. J. Chen *et al.*, *Proc. Natl. Acad. Sci. U.S.A.* **100**, 4984 (2003).
30. R. J. Chen *et al.*, *J. Am. Chem. Soc.* **126**, 1563 (2004).
31. S. O. Meroueh *et al.*, *Proc. Natl. Acad. Sci. U.S.A.* **103**, 4404 (2006).
32. J. Kong *et al.*, *Science* **287**, 622 (2000).
33. P. G. Collins, K. Bradley, M. Ishigami, A. Zettl, *Science* **287**, 1801 (2000).
34. T. Zhang, S. Mubeen, N. V. Myung, M. A. Deshusses, *Nanotechnology* **19**, 332001 (2008).
35. A. Tsugita, M. Inouye, E. Terzaghi, G. Streisin, *J. Biol. Chem.* **243**, 391 (1968).
36. H. B. Jensen, K. Kleppe, *Eur. J. Biochem.* **28**, 116 (1972).
37. Y. Chen, D. Hu, E. R. Vorpagel, H. P. Lu, *J. Phys. Chem. B* **107**, 7947 (2003).
38. S. N. Xie, *Single Molecules* **2**, 229 (2001).
39. H. P. Lu, L. Y. Xun, X. S. Xie, *Science* **282**, 1877 (1998).
40. D. Hu, H. P. Lu, *Biophys. J.* **87**, 656 (2004).
41. H. P. Lu, *Curr. Pharm. Biotechnol.* **5**, 261 (2004).
42. Y. Wang, H. P. Lu, *J. Phys. Chem. B* **114**, 6669 (2010).
43. G. E. Arnold, J. I. Manchester, B. D. Townsend, R. L. Ornstein, *J. Biomol. Struct. Dyn.* **12**, 457 (1994).
44. B. L. de Groot, S. Hayward, D. M. F. van Aalten, A. Amadei, H. J. C. Berendsen, *Proteins* **31**, 116 (1998).
45. H. R. Faber, B. W. Matthews, *Nature* **348**, 263 (1990).
46. K. Svoboda, P. P. Mitra, S. M. Block, *Proc. Natl. Acad. Sci. U.S.A.* **91**, 11782 (1994).
47. M. J. Schnitzer, S. M. Block, *Cold Spring Harb. Symp. Quant. Biol.* **60**, 793 (1995).
48. W. L. Xu, J. S. Kong, P. Chen, *J. Phys. Chem. C* **113**, 2393 (2009).
49. M. J. Schnitzer, S. M. Block, *Nature* **388**, 386 (1997).
50. G. Bhabha *et al.*, *Science* **332**, 234 (2011).
51. H. S. Mchaourab, K. J. Oh, C. J. Fang, W. L. Hubbell, *Biochemistry* **36**, 307 (1997).
52. E. Stern *et al.*, *Nano Lett.* **7**, 3405 (2007).
53. I. Heller *et al.*, *Nano Lett.* **8**, 591 (2008).
54. L. Prisbrey, G. Schneider, E. Minot, *J. Phys. Chem. B* **114**, 3330 (2010).
55. C. Li *et al.*, *J. Am. Chem. Soc.* **127**, 12484 (2005).
56. S. R. Hunt, D. Wan, V. R. Khalap, B. L. Corso, P. G. Collins, *Nano Lett.* **11**, 1055 (2011).
57. B. Brooks, M. Karplus, *Proc. Natl. Acad. Sci. U.S.A.* **82**, 4995 (1985).

Acknowledgments: This work was sponsored by the National Cancer Institute of the NIH (R01 CA133592-01 and T32CA009054) and NSF (DMR-0801271, ECCS-0802077, and the Center for Chemical Innovation on Chemistry at the Space-Time Limit CHE-0802913).

Supporting Online Material

www.sciencemag.org/cgi/content/full/335/6066/319/DC1
Materials and Methods
SOM Text
Figs. S1 to S6
Tables S1 and S2
References (*58*–*74*)

4 October 2011; accepted 5 December 2011
10.1126/science.1214824

Destruction of Sun-Grazing Comet C/2011 N3 (SOHO) Within the Low Solar Corona

C. J. Schrijver,[1]* J. C. Brown,[2] K. Battams,[3] P. Saint-Hilaire,[4] W. Liu,[1,5] H. Hudson,[2,4] W. D. Pesnell[6]

Observations of comets in Sun-grazing orbits that survive solar insolation long enough to penetrate into the Sun's inner corona provide information on the solar atmosphere and magnetic field as well as on the makeup of the comet. On 6 July 2011, the Solar Dynamics Observatory (SDO) observed the demise of comet C/2011 N3 (SOHO) within the low solar corona in five wavelength bands in the extreme ultraviolet (EUV). The comet penetrated to within 0.146 solar radius (~100,000 kilometers) of the solar surface before its EUV signal disappeared. Before that, material released into the coma—at first seen in absorption—formed a variable EUV-bright tail. During the final 10 minutes of observation by SDO's Atmospheric Imaging Assembly, ~6×10^8 to 6×10^{10} grams of total mass was lost (corresponding to an effective nucleus diameter of ~10 to 50 meters), as estimated from the tail's deceleration due to interaction with the surrounding coronal material; the EUV absorption by the comet and the brightness of the tail suggest that the mass was at the high end of this range. These observations provide evidence that the nucleus had broken up into a family of fragments, resulting in accelerated sublimation in the Sun's intense radiation field.

During its 15 years of operation, the Large Angle and Spectrometric Coronagraph (LASCO) (*1*) onboard the Solar and Heliospheric Observatory (SOHO) has observed more than 2000 comets as they approached the Sun. The population of Sun-grazing comets is dominated by the Kreutz group, which orbit to within one to two solar radii from the solar surface with orbital periods of 500 to 1000 years. More than 1400 of the comets seen by SOHO are members of this group, making it the largest known group of comets, likely originating from the breakup of a progenitor body as recently as 2500 years ago (*2*). Only the largest of the Kreutz-group comets [with diameters up to ~100 m (*2*)] have survived closest approach (perihelion), and SOHO never witnessed such a survival (*3*) until sungrazing comet Lovejoy emerged after its perihelion passage on the Sun's far side on 15–16 December 2011. Most of the destructions occurred well before perihelion, but some occurred after the comet disappeared behind the occulting disk of the coronagraph. None could be followed into the Sun's lower atmosphere.

Here, we report on the observed destruction of comet C/2011 N3 (SOHO) within the solar atmosphere. We use EUV images obtained with the Atmospheric Imaging Assembly [AIA (*4*)] on the Solar Dynamics Observatory (SDO), which show different parts of the comet in absorption and in emission against the background EUV emission from the hot (1×10^6 to 3×10^6 K) outer solar atmosphere (the corona). AIA images the entire visible hemisphere of the Sun, including its off-disk corona, at 12-s intervals for sets of eight distinct (E)UV channels, at a resolution of ~1.2 arc sec, and with a high signal-to-noise ratio achieved with exposures no longer than 2.3 s. The comet's speed of ~600 km/s caused blurring in the AIA exposures that is only slightly in excess of the instrumental resolution. This detailed view of the solar corona enabled us to track the comet's tail and to determine the comet's orbit across much of the solar disk until it faded within 20 min of its first appearance. From Fig. 1 and movies S1 and S2, it appears that the comet's nucleus had fragmented.

The comet C/2011 N3 (SOHO) was first seen in AIA's 171 Å EUV channel while it was ~0.2 solar radii in projection off the solar limb, roughly at 5 July 2011 23:46 UTC (all times are given in UTC for photon arrival times at SDO, in geosynchronous orbit). The comet could be tracked in AIA images until approximately 6 July 2011 00:05:50, when it faded from all five EUV channels in which it was visible (131, 171, 193, 211, and 335 Å). Observations made by the Extreme-Ultraviolet Imager (EUVI) on the Solar-Terrestrial Relations Observatory [STEREO (*5*)] B show a faint signal of the comet high above the solar surface from its near-quadrature view relative to the Sun-Earth line (and thus against a background coronal emission weaker than from AIA's perspective by nearly a factor of 10) up to

[1]Lockheed Martin Advanced Technology Center, 3251 Hanover Street, Palo Alto, CA 94304, USA. [2]School of Physics and Astronomy, University of Glasgow, Glasgow G12 8QQ, UK. [3]Naval Research Laboratory, Code 7663, 4555 Overlook Avenue, SW, Washington, DC 20375, USA. [4]Space Sciences Laboratory, University of California, Berkeley, CA 94720, USA. [5]W. W. Hansen Experimental Physics Laboratory, Stanford University, Stanford, CA 94305, USA. [6]Code 671, NASA Goddard Space Flight Center, Greenbelt, MD 20771, USA.

*To whom correspondence should be addressed. E-mail: schrijver@lmsal.com